

THE X-RAY POWER SPECTRAL DENSITY FUNCTION AND BLACK HOLE MASS ESTIMATE FOR THE SEYFERT AGN IC 4329A

A. MARKOWITZ

Center for Astrophysics and Space Sciences, University of California, San Diego, M.C. 0424, La Jolla, CA, 92093-0424, USA

ABSTRACT

We present the X-ray broadband power spectral density function (PSD) of the X-ray-luminous Seyfert IC 4329a, constructed from light curves obtained via *Rossi X-ray Timing Explorer* monitoring and an *XMM-Newton* observation. Modeling the 3–10 keV PSD using a broken power-law PSD shape, a break in power-law slope is significantly detected at a temporal frequency of $2.5_{-1.7}^{+2.5} \times 10^{-6}$ Hz, which corresponds to a PSD break time scale T_b of $4.6_{-2.3}^{+10.1}$ days. Using the relation between T_b , black hole mass M_{BH} , and bolometric luminosity as quantified by McHardy and coworkers, we infer a black hole mass estimate of $M_{\text{BH}} = 1.3_{-0.3}^{+1.0} \times 10^8 M_{\odot}$ and an accretion rate relative to Eddington of $0.21_{-0.10}^{+0.06}$ for this source. Our estimate of M_{BH} is consistent with other estimates, including that derived by the relation between M_{BH} and stellar velocity dispersion. We also present PSDs for the 10–20 and 20–40 keV bands; they lack sufficient temporal frequency coverage to reveal a significant break, but are consistent with the same PSD shape and break frequency as in the 3–10 keV band.

Subject headings: galaxies: active — galaxies: Seyfert — X-rays: galaxies — galaxies: individual (IC 4329a)

1. INTRODUCTION

The rapidly variable, aperiodic X-ray continuum emission from Seyfert AGN has long supported the notion that the X-ray emission originates from within a few tens of Schwarzschild radii of the central supermassive black hole. In the late 1980's, *EXOSAT* probed X-ray variability on time scales of a few days or less, yielding power spectral density functions (PSDs) covering temporal frequencies down to $\sim 10^{-5}$ Hz. These PSDs established the scale-invariant "red-noise" nature, i.e., larger variability amplitudes toward larger time scales, characterized by a PSD which increases toward lower temporal frequencies. However, no characteristic time scale, such as a "break" in the PSD power-law slope, was detected (e.g., Lawrence et al. 1987; McHardy & Czerny 1987; Green, McHardy & Lehto 1993).

The *Rossi X-ray Timing Explorer (RXTE)* was launched in 1995; its unique attributes (large effective area, high throughput, fast slewing, and flexible scheduling) permitted multi-time scale monitoring campaigns that probed X-ray variability on time scales from hours to years (temporal frequencies from 10^{-4} – 10^{-8} Hz). The resulting Seyfert broadband PSDs yielded evidence for breaks at temporal frequencies f_b with PSD power-law slopes breaking from ~ -2 to ~ -1 above and below f_b , respectively; the break frequencies corresponded to break time scales T_b of a few days or less (e.g., Edelson & Nandra 1999; Pounds et al. 2001; Uttley, McHardy & Papadakis 2002 (hereafter U02); Markowitz et al. 2003b (hereafter M03); Papadakis, Reig & Nandra 2003; McHardy et al. 2004, 2005; Uttley & McHardy 2005).

It was noted by M03 that a small sample of Seyfert PSDs was consistent with a relation between T_b and black hole mass M_{BH} estimated via reverberation mapping, in the sense that relatively larger-mass black holes are associated with PSDs with larger values of T_b , albeit with some scatter. Using a larger sample, McHardy et al. (2006) demonstrated that the scatter could be explained

by an additional dependence of T_b on $L_{\text{Bol}}/L_{\text{Edd}}$, the accretion rate relative to Eddington, in that for a given M_{BH} , sources accreting at relatively higher rates have PSDs shifted toward higher f_b (smaller values of T_b). In the absence of an accurate estimate of M_{BH} by other means, X-ray timing can thus be used to estimate M_{BH} , if T_b and bolometric luminosity L_{Bol} are both known.

In this paper, we present the broadband 3–10 keV PSD of IC 4329a, an X-ray bright and variable Seyfert located at a redshift of $z = 0.01605$ (Willmer et al. 1991). IC 4329a had been monitored in the optical with the intent of using reverberation mapping to estimate M_{BH} in this object, but the constraints were quite poor (Winge et al. 1996; Peterson et al. 2004). Here, we demonstrate that there is significant evidence for a break in the X-ray PSD of IC 4329a. We also present PSDs for the 3–5, 5–10, 10–20, and 20–40 keV bands. Section 2 reviews the multi-time scale sampling strategy and describes the observations, data reduction, and light curve sampling. Section 3 describes the methods of measurement and modeling of the PSDs. The results of model fits to the PSDs are presented in §4. In §5, the PSD break frequency is used to yield an estimate of M_{BH} based on X-ray timing, which we compare to estimates obtained by various other methods.

2. OBSERVING STRATEGY, OBSERVATIONS, AND DATA REDUCTION

We followed the observing strategy of Edelson and Nandra (1999), U02, M03, etc., in which a source is monitored with even, regular sampling on multiple time scales such that the resulting set of light curves yields individual PSDs covering complementary temporal frequency ranges. With the reasonable assumption that the underlying PSD shape has remained constant throughout all the monitoring observations¹, the individual PSDs are

¹ The X-ray PSDs of black hole X-ray Binaries are observed to vary (display strong non-stationarity) on time scales of hours to

combined to produce the final broadband PSD.

IC 4329a was monitored with *RXTE* once every 4.26 days (64 orbits) for a duration of 4.3 years, from 2003 Apr 8 to 2007 Aug 7 (Modified Julian Day (MJD) 52737–54319; observation identifiers 80152-03-*, 90154-01-*, 91138-01-*, and 92108-01-*). This sampling, which probes variability on time scales from \sim a week to a few years, is henceforth called “long-term” sampling. Each observation lasted approximately 1 ks. There were four gaps due to sun-angle constraints in October–November of each year; each gap was \sim 50 days long. More intensive monitoring with *RXTE* was done to probe variability on time scales from several hours to a month (“medium-term” sampling). *RXTE* observed IC 4329a once every \sim 17.1 ks (three orbits) for a duration of 34.1 days, from 2003 Jul 10 at 18:05 UT to 2003 Aug 13 at 20:35 UT (MJD 52830.75–52864.86; observation identifiers 80152-04-*). Again, each visit lasted \sim 1 ks. Finally, a continuous, 133 ks observation of IC 4329a with *XMM-Newton* (§2.3) allowed us to probe variability on time scales from \sim an hour to 1 day.

2.1. PCA data reduction

The Proportional Counter Array (PCA; Swank 1998) consists of five large-area, collimated proportional counter units (PCUs). Reduction of the PCA data followed standard extraction and screening procedures, using HEASOFT version 6.5.1 software. PCA STANDARD-2 data were collected from PCU 2 only; PCUs 1, 3 and 4 have been known to suffer from repeated breakdown during on-source time, and PCU 0 lost its propane veto layer in 2000. Data were rejected if they were gathered less than 10° from the Earth’s limb, within 30 minutes of satellite passage through the South Atlantic Anomaly (SAA), if the satellite’s pointing offset was greater than 0.2° , or if ELECTRON2 was > 0.1). As the PCA is a non-imaging instrument, the background was estimated using the “L7-240” background models, appropriate for faint sources; see e.g., Markowitz, Edelson & Vaughan (2003a) and Edelson & Nandra (1999) for details on PCA background subtraction, the dominant source of systematic uncertainty (e.g., in total broadband count rate) in these data. Spectral fitting for each observation was done using XSPEC version 11.3.2ag, assuming a Galactic column of $4.6 \times 10^{20} \text{ cm}^{-2}$ (Kalberla et al. 2005). As the response of the PCA slowly hardens slightly over time due to the gradual leak of xenon gas into the propane layer in each PCU,² response files were generated for each separate observation. Fluxed light curves were extracted in the 3–10 keV band by fitting a power-law to that band only (2–10 keV is a “standard” hard X-ray measurement band, but the 2–3 keV effective area of the PCA is extremely small, so we use 3–10 keV here). Light curves for the 3–5 and 5–10 keV sub-bands and the 10–20 keV band were also extracted. Errors on each light curve point were derived from the standard error of 16-s count rate light curve bins within each observation. The total number of data points after

days and longer. Scaling with M_{BH} and/or X-ray luminosity, we expect significant changes in the shapes of AGN PSDs only on timescales of centuries to millennia.

² In two previous papers, Markowitz, Reeves & Braito (2006) and Markowitz et al. (2009), the cause of the evolution in response was incorrectly listed as propane leaking into the xenon layers.

screening was 372 points for each long-term light curve, with 14.5% of the data missing due to, e.g., sun-angle constraints or screening. Each medium-term light curve contained 173 points, with only 4.1% of the data missing. The 3–10 keV light curves are plotted in Figure 1.

We also extracted 20–40 keV PCA light curves, as it would have been desirable to have PCA data simultaneous with the 20–40 keV High-Energy X-Ray Timing Experiment (HEXTE) light curves (see below), but in this band, the source was only \sim 7% of the total PCA background; \pm 2% systematic uncertainties in the PCA background on time scales of \sim 1–2 ks (Jahoda et al. 2006, Figure 29) yield uncertainties of $\sim \pm$ 30% uncertainties in the net source count rate, and so we do not consider the PCA above 20 keV.

2.2. HEXTE data reduction

The High-Energy X-Ray Timing Experiment (HEXTE) aboard *RXTE* consists of two independent clusters (A and B), each containing four NaI(Tl)/CsI(Na) phoswich scintillation counters (see Rothschild et al. 1998) which share a common 1° FWHM field of view. Each of the eight detectors has a net open area of about 200 cm^2 . Source and background spectra were extracted from each individual *RXTE* visit using Science Event data and standard extraction procedures. The same good time intervals used for the PCA data (e.g., Earth elevation and SAA passage screening) were applied to the HEXTE data. To measure real-time background measurements, the two HEXTE clusters each undergo two-sided rocking to offset positions, in this case, to 1.5° off-source, switching every 32 s. There is a galaxy cluster (Abell 3571, located at a redshift of $z = 0.039$) located about 2° south of IC 4329a, at R.A. = 13h 47.5m, decl. = $-32^\circ 52 \text{ m}$. This source is detected in the *RXTE* all-sky slew survey (XSS; Revnivtsev et al. 2004), which shows the 8–20 keV flux of this source to be about half that of IC 4329a (at 2° off-axis, the count rate in the PCA is negligible, and thus the effect of contamination from Abell 3571 on PCA light curves and PSDs is negligible; Jahoda et al. 2006). However, *BeppoSAX*-PDS observations have shown no detection of Abell 3571 above 15 keV (Nevalainen et al. 2004). The 8–20 keV emission seen by the XSS must therefore be emission only between 8 and \lesssim 15 keV, and in this paper we use the 20–40 keV band, so the presence of A3571 can be safely ignored as far as contaminating HEXTE background data obtained within \sim 1– 2° of the center of A3571 is concerned. Cluster A data taken during the following times were excluded, as the cluster did not rock on/off-source: 2004 Dec 13 – 2005 Jan 14, 2005 Dec 12 – 2006 Jan 4, during 2006 Jan 25, and after 2006 Mar 14. Detector 2 aboard cluster B lost spectral capabilities in 1996; these data were excluded. Light curves were extracted in 16 s bins in the 20–40 keV band. Deadtime corrections were applied to account for cluster rocking, pulse analyzer electronics, and the recovery time following scintillation pulses caused by high-energy charged particles; typically, the HEXTE deadtime is \sim 30 – 40%. The light curves were then binned to every 12.79 days (long-term) or 50.2 ks (medium-term). This action minimized variability associated with background systematics. The HEXTE background is relatively stable over long time scales but rapidly variable within

a single satellite orbit as the spacecraft moves in the geomagnetic environment. For a typical background rate, the Poisson error in a ~ 600 s good time exposure is $\gtrsim 1\%$ (Gruber et al. 1996). In the case of IC 4329a, the net source flux is roughly 9% of the total background in the 20–40 keV band, and each observation was only 1 ks in duration, yielding a $\gtrsim 10\%$ systematic uncertainty in the net source count rate. In addition, there are likely systematic uncertainties associated with the deadtime correction, $\lesssim 0.5\%$ in a 1 ks duration observation³. Errors on each point were determined by the standard error of the 16 s points. For observations using both clusters, light curves from clusters A and B were added; all light curves are in units of $\text{ct s}^{-1} \text{ detector}^{-1}$ (that is, ct s^{-1} per 7 detectors when both clusters were in operation, or per 3 detectors when only cluster B was operating normally; there were no observations where cluster A was the only cluster operating normally). The long-term light curve had 125 points, with 13 points (10.4%) missing; the medium-term light curve had 60 points, with no points missing.

The 20–40 keV light curves are plotted in Figure 1. The HEXTE gain and response are both very stable over time scales of years, permitting us to work in units of count rates. However, the HEXTE light curves, plotted in Figure 1, have had count rates converted to fluxes for consistency with the way the PCA light curves are plotted; we use a conversion rate of 1 ct s^{-1} per HEXTE detector in 20–40 keV corresponding to $2.6 \times 10^{-10} \text{ erg cm}^{-2} \text{ s}^{-1}$ for a source with a photon index of 1.7. Visually, there appears to be some mild variability in the 20–40 keV light curves not present in the 3–10 keV light curve, likely from the aforementioned systematic uncertainties associated with background subtraction and deadtime correction. However, we note that the overall shape of the resulting long- and medium-term combined PSD (see §4) is roughly consistent with that obtained for the 10–20 keV band at the temporal frequencies probed, and we are confident that the systematic effects associated with HEXTE background subtraction and deadtime correction do not significantly affect our conclusions for the 20–40 keV PSD.

2.3. XMM-Newton data reduction

XMM-Newton observed the nucleus of IC 4329a during 2003 Aug 6–7 (observation identifier 0147440101), for a duration of 136 ks. In this paper, we only consider data collected using the European Photon Imaging Camera (EPIC) pn camera. Light curves were extracted using XMM Science Analysis Software version 7.1.0, XSELECT version 2.4a, and the latest calibration files. Source photons were extracted from a circular region of radius $40''$; backgrounds were extracted from circles of identical size, centered $\sim 3'$ away from the core. Hot, flickering, or bad pixels were excluded. We inspected the 10–13 keV pn background light curve for flares, and excluded periods when the 10–13 keV background rate exceeded 0.1 ct s^{-1} . We extracted a light curve in the 3–10 keV band binned to 2000 s; variability at shorter time scales was dominated by Poisson noise. The light curve had 67 points, with 3 points, or 4.5%, missing due to the above background screening. It is

plotted in Figure 1. Light curves for the 3–5 and 5–10 keV sub-bands were also extracted, binned to 5000 s (27 points).

3. PSD MEASUREMENT

Light curve sampling parameters, including mean net source and background count rates, for all light curves are listed in Table 1. Also listed in Table 1 are variability amplitudes F_{var} (see Vaughan et al. 2003 for definition of F_{var} and its uncertainty) for all light curves. Previous works have noted that, from 2 to ~ 20 keV, F_{var} is generally observed to decrease with increasing photon energy (e.g., Markowitz, Edelson & Vaughan 2003a; Miniutti et al. 2007); possible explanations include the dilution of the observed variability of the coronal power-law component by the Compton reflection hump or “pivoting” of the power-law component. The values of F_{var} for the 3–5, 5–10, and 10–20 keV bands are consistent with this trend (in the case of the 20–40 keV light curve, it is not immediately obvious how much variability is intrinsic and how much is due to the systematic effects discussed in §2). Table 2 lists PSD measurement parameters. The 3–10 keV band has the best temporal frequency coverage; this band and the 3–5 and 5–10 keV sub-bands each contain long-, medium- and short-term sampling. As XMM-Newton lacks coverage above 12 keV, there is no short-term sampling to complement the 10–20 keV and 20–40 keV PSDs. Nonetheless, the 20–40 keV PSD presented here is, to our knowledge, the first X-ray PSD of a Seyfert above 20 keV.

PSDs were measured for each light curve separately, as described in §3.1. However, as described in §3.2, these “observed” PSDs suffer from measurement distortion effects (aliasing and red-noise leak) and the errors are not well-determined. A model-dependent Monte Carlo method was used to assign proper errors and to recover the intrinsic, underlying PSD shape. These steps are reviewed only briefly in the next two subsections; for further details, the reader is referred to U02 and M03.

3.1. Initial PSD construction

Initial PSD construction closely followed §3.1 of M03. Light curves were linearly interpolated across gaps, though such gaps were rare. Each light curve’s mean was subtracted. Periodograms were constructed using a Discrete Fourier Transform (e.g., Oppenheim & Shafer 1975; see also §3.1 of M03 for definitions of Fourier frequencies f and the periodogram).

Following Papadakis & Lawrence (1993) and Vaughan (2005), the periodogram was logarithmically binned every factor of 1.6 in f (0.20 in the logarithm) to produce the observed PSD $P(f)$; the two lowest temporal frequency bins were widened to accommodate three periodogram points. The ~ 5 lowest-temporal frequency bins in each individual PSD typically contained < 15 periodogram points, precluding us from assigning normal errors.

The individual long-, medium-, and short-term PSDs were combined to yield the final, broadband observed PSDs $P(f)$, which are plotted in Figure 2, as well as in the top panels of Figures 3, 4, and 5 in $f \times P_f$ space. No renormalization of the individual PSDs was done. The constant level of power due to Poisson noise was

³ See http://mamacass.ucsd.edu/hexte/status/hexte_deadtime.html

not subtracted from these PSDs, but instead modeled in the Monte Carlo analysis below.

3.2. Monte Carlo Simulations

Visual inspection of Figure 2 supports, at first glance, the notion that all five PSDs are at least roughly consistent in broadband shape. However, to account for PSD measurement effects (the reader is referred to U02 and M03 for descriptions of aliasing and red-noise leak, and how the method accounts for them) and to assign proper errors, we use a version of the Monte Carlo technique “PSRESP” introduced by U02. We summarize this technique as follows: one first assumes an underlying broadband model PSD shape, and, for each individual observed light curve sampling pattern, one uses the algorithm of Timmer & König (1995) to generate N_{trial} light curves. The simulated light curves are each resampled to match the observed light curve, then PSDs are calculated. The model average PSD $\overline{P_{\text{sim}}(f)}$, which accounts for the distortion effects, is calculated from the N_{trial} PSDs; errors for each PSD bin are assigned based on the RMS spread of the individual simulated PSDs at a given temporal frequency bin. The constant level of power due to Poisson noise P_{psn} (see Table 2) is added to the model as $P_{\text{psn}} = 2(\mu + B)/\mu^2$, where μ and B are the source and background count rates, respectively; for non-continuously sampled light curves, this must be multiplied by the ratio of ΔT_{samp} , the average sampling time, to the average exposure time per observation. For the HEXTE light curves, the estimates of P_{psn} were calculated taking into consideration the total number of good detectors (e.g., times when cluster A data were not used).

The goodness of fit is determined. A statistic χ_{dist}^2 which compares the observed PSD $P(f)$ to the model average PSD $\overline{P_{\text{sim}}(f)}$, using the errors from the model (as opposed to using poorly-determined errors from the observed PSD), is calculated. The best-fitting normalization of the $P_{\text{sim}}(f)$ is found by renormalizing $\overline{P_{\text{sim}}(f)}$ until the value of observed χ_{dist}^2 is minimized. 10,000 combinations of the long-, medium-, and short-term PSDs $P_{\text{sim}}(f)$ are randomly selected to model the χ_{dist}^2 distribution, comparing $P_{\text{sim}}(f)$ to $\overline{P_{\text{sim}}(f)}$. The probability that the model PSD can be rejected, R , is defined as the percentile of the 10,000 simulated χ_{dist}^2 values exceeded by the value of the observed χ_{dist}^2 .

A range of underlying PSD model shapes is thus tested in this way, and the model with the lowest rejection probability (highest likelihood of acceptance $L \equiv 1 - R$) can be identified.

4. PSD FIT RESULTS

We tested PSD model shapes consisting of simple unbroken power-law models and singly-broken power-law models; the quality of each PSD precludes more complex shapes such as single or multiple Lorentzian components or quasi-periodic oscillations routinely modeled in the PSDs of X-ray Binary systems.

The unbroken power-law model was of the form $P(f) = A_0(f/f_0)^{-\alpha}$, where α is the power-law slope and the normalization A_0 is the PSD amplitude at f_0 , arbitrary chosen to be 10^{-6} Hz. P_{psn} is added to each simulated PSD but is not explicitly listed here since P_{psn} is different for

each PSD segment. The model was tested by stepping through α from 0.0 to 3.2 in increments of 0.1, each time with $N_{\text{trial}}=300$ simulations done to calculate $\overline{P_{\text{sim}}(f)}$. The best-fitting models are plotted in the second panels of Figures 3, 4 and 5. The best-fitting values of α , A_0 , and likelihood of acceptance L_{unbr} are listed in Table 3. The errors on α correspond to values 1σ above the rejection probability R_{unbr} for the best-fit value on a Gaussian probability distribution; for example, if the best-fit model had $R_{\text{unbr}}=95.45\%$ (2.0σ on a Gaussian probability distribution), errors correspond to $R_{\text{unbr}}=99.73\%$ (3.0σ). The errors on A_0 were determined from the RMS spread of the 10^4 randomly selected sets of simulated PSDs.

The high rejection probabilities for the 3–10, 3–5, and 5–10 keV PSDs (each $> 90\%$) and the residuals plotted in Figures 3b and 4b suggest that a more complex PSD model shape may be appropriate for these three PSDs. The 10–20 keV and 20–40 keV PSDs cover less dynamic range in temporal frequency than their <10 keV counterparts due to the lack of short-term sampling; the rejection probabilities are consequently much lower, $<90\%$, along with smaller residuals (Figure 5b).

To test for the presence of breaks in the PSD, we then tested a singly-broken PSD model shape of the form

$$P(f) = \begin{cases} A_1(f/f_b)^{-\alpha_{\text{lo}}}, & f \leq f_b \\ A_1(f/f_b)^{-\alpha_{\text{hi}}}, & f > f_b \end{cases}$$

where the normalization A_1 is the PSD amplitude at the break frequency f_b , and α_{lo} and α_{hi} are the low- and high-frequency power law slopes, respectively, with the constraint $\alpha_{\text{lo}} < \alpha_{\text{hi}}$. (We also tested a more slowly-bending PSD model of the form $P(f) = (A_1 f^{-\alpha_{\text{lo}}}) / ((1 + f/f_b)^{(\alpha_{\text{hi}} - \alpha_{\text{lo}})})$, but given the PSD quality, there were degeneracies between f_b , α_{lo} , and α_{hi} such that reasonable constraints on f_b could not be attained.) The range of slopes tested was 0.0–3.2 in increments of 0.1. Break frequencies were tested in the log from -7.4 to -4.9 in increments of 0.1, corresponding to $f \rightarrow 1.26f$ in the linear scale. 100 simulated PSDs were used to determine $\overline{P_{\text{sim}}(f)}$. The best-fit model parameters, along with likelihoods of acceptance L_{brkn} , are listed in Table 4; residuals are plotted in the bottom panels of Figures 3 and 4 for the 3–10, 3–5, and 5–10 keV PSDs. Figure 6 shows contour plots of α_{hi} versus f_b for these three PSDs at the respective best-fit values of α_{lo} . We use the ratio of the likelihoods of acceptance $L_{\text{brkn}}/L_{\text{unbr}}$ between the broken and unbroken power law model fits to establish if a break is significant (we use $L_{\text{brkn}}/L_{\text{unbr}}$ at least ~ 10). For the 3–10 keV PSD, we conclude that a break is significantly detected at $f_b = 10^{-(5.6(+0.5, -0.3))}$ Hz = $2.51_{-1.72}^{+2.50} \times 10^{-6}$ Hz, which corresponds to a time scale of $4.6_{-2.3}^{+10.1}$ days. Breaks are also significantly detected in each 3–5 and 5–10 keV sub-band PSD, with best values of f_b also near 10^{-6} Hz. Because of the limited dynamic range in temporal frequency for the 10–20 and 20–40 keV PSDs, the improvement in fit when adding a break to the model is not high, with $L_{\text{brkn}}/L_{\text{unbr}} \sim 2 - 3$. Parameters for the broken power-law model are thus listed in parentheses in Table 4 for these two PSDs and data/model residuals are not plotted.

We next explored the possibility that all five PSDs

could be consistent with the same PSD shape, namely that of the 3–10 keV PSD, with a low-frequency power law slope equal to -1.0 , a high frequency slope near -2 , and a break frequency $\sim 1 - 2 \times 10^{-6}$ Hz. We re-tested the 3–5 and 5–10 keV PSDs with a broken power-law model, keeping α_{10} fixed at 1.0. Acceptable fits were obtained, with best-fit values for f_b and α_{hi} consistent with those measured for the 3–10 keV PSD; results are listed in Table 4. The 10–20 and 20–40 keV PSDs only cover up to roughly 10^{-5} Hz, and there is not much “leverage” above $\sim 10^{-5.5-6}$ Hz to either confirm or refute the presence of a break at those temporal frequencies. However, the best-fit power law slopes in the unbroken power law fits are flat, 1.1–1.2 (compared to 1.5–1.7 for the < 10 keV PSDs, which extend up to roughly 10^{-4} Hz, well above the best-fit 3–10 keV PSD break frequency). We conclude that the 10–20 and 20–40 keV PSDs are at least roughly consistent with the presence of breaks at or near that found in the < 10 keV PSDs, and with the same α_{10} , and that the > 10 keV PSDs probe temporal frequencies primarily below the break frequency.

5. DISCUSSION AND CONCLUSIONS

5.1. A New Black Hole Mass Estimate for IC 4329a from X-ray Timing

We have used complementary *RXTE* and *XMM-Newton* monitoring of the X-ray bright Seyfert AGN IC 4329a to measure the 3–10 keV PSD, and we find significant evidence for a break in the modeled power-law slope at a temporal frequency of $2.5_{-1.7}^{+2.5} \times 10^{-6}$ Hz, which corresponds to a break time scale T_b of $4.6_{-2.3}^{+10.1}$ days. Best-fit power law slopes above and below the break are $\alpha_{hi} = 2.3_{-0.4}^{+0.8}$ and $\alpha_{10} = 1.0_{-0.3}^{+0.4}$, respectively. For a discussion of candidate physical mechanisms to explain the turnover, the reader is referred to, e.g., Edelson &andra (1999) and Arévalo & Uttley (2006).

We can derive a new estimate for M_{BH} from the PSD break, using the empirical relation between T_b , bolometric luminosity L_{Bol} , and M_{BH} quantified by McHardy et al. (2006), $\log(T_b(\text{days})) = 2.1 \log(M_{BH}/10^6 M_\odot) - 0.98 \log(L_{Bol}/10^{44} \text{ erg s}^{-1}) - 2.32$. The average absorbed 3–10 keV flux from the long-term PCA monitoring is $11.18 \times 10^{-11} \text{ erg cm}^{-2} \text{ s}^{-1}$. To find the unabsorbed flux, we used a spectral model in XSPEC consisting of a power law with photon index 1.74 (Markowitz, Reeves & Braitto 2006), absorbed by the Galactic column, and five layers of absorption modeled by Steenbrugge et al. (2005): a column of cold gas intrinsic to the host galaxy with column density $N_H = 1.7 \times 10^{21} \text{ cm}^{-2}$, and four ionized absorbers, with column densities 1.3, 0.32, 6, and $2 \times 10^{21} \text{ cm}^{-2}$ and ionization parameters $\log \xi^4 = -1.37, 0.56, 1.92, \text{ and } 2.70 \text{ erg cm s}^{-1}$, respectively. (A fifth ionized absorber quantified by Markowitz, Reeves & Braitto 2006, with best-fit modeled values of $\log \xi = 3.73 \text{ erg cm s}^{-1}$ and $N_H = 1.4 \times 10^{22} \text{ cm}^{-2}$, is expected to produce only a narrow Fe K absorption feature and is ignored.) To model each ionized absorber, an XSTAR component was used (Bautista & Kallman 2001). Using

this model, a luminosity distance of 78.6 Mpc (Mould et al. 2000), and assuming a cosmology with $H_0 = 70 \text{ km s}^{-1} \text{ Mpc}^{-1}$ and $\Lambda_0 = 0.73$, the unabsorbed, rest-frame 2–10 keV luminosity L_{2-10} is thus estimated to be $1.1 \times 10^{44} \text{ erg s}^{-1}$. Using Marconi et al. (2004, their Figure 3b), $L_{bol}/L_{2-10} = 30$, and $L_{bol} = 3.3 \times 10^{45} \text{ erg s}^{-1}$. Using the relation of McHardy et al. (2006), we derive $M_{BH} = 1.3_{-0.3}^{+1.0} \times 10^8 M_\odot$ (a 7% uncertainty in the distance to IC 4329a (Mould et al. 2000) translates into an additional $\sim 7\%$ uncertainty on M_{BH}). The accretion rate relative to Eddington, L_{Bol}/L_{Edd} , is thus estimated to be $0.21_{-0.10}^{+0.06}$.

This estimate of M_{BH} is in agreement with several estimates obtained by other methods. Reverberation mapping has been known to yield highly accurate estimates of M_{BH} , but only if the data are of sufficiently high quality. In the case of IC 4329a, the estimate of M_{BH} is poorly constrained due to relatively low-quality optical spectra, and formally only an upper limit, $9.90_{-11.88}^{+17.88} \times 10^6 M_\odot$ (see Peterson et al. 2004 for details). However, many other methods of estimating M_{BH} in IC 4329a yield estimates closer to $\sim 10^8 M_\odot$. This includes other methods based on estimating the distance R_{BLR} from the central continuum source to the Broad Line Region, such as the empirical relation noted by Kaspi et al. (2000) between R_{BLR} and the optical continuum luminosity, “recalibrated” by Vestergaard & Peterson (2006; their equation 5). Using the value of H β FWHM (RMS) from Wandel, Peterson & Malkan (1999), $5960 \pm 2070 \text{ km s}^{-1}$, and a value for $\lambda L_\lambda(5100\text{\AA})$ of $1.64 \pm 0.21 \times 10^{41} \text{ erg s}^{-1}$ from Kaspi et al. (2000), the Vestergaard & Peterson (2006) equation yields $M_{BH} = 1.2_{-0.7}^{+1.4} \times 10^8 M_\odot$. Vestergaard & Peterson (2006; their equation 6) also provide a recalibrated formula for estimates of M_{BH} based on H β luminosity and optical continuum luminosity. Winge et al. (1996) report a mean H β flux of $3.331 \times 10^{-13} \text{ erg cm}^{-2} \text{ s}^{-1}$; assuming a luminosity distance of $78.6 \pm 5.5 \text{ Mpc}$ (Mould et al. 2000) yields an H β luminosity of $2.45_{-0.31}^{+0.36} \times 10^{41} \text{ erg s}^{-1}$. The resulting estimate of M_{BH} is thus $6.8_{-4.3}^{+7.7} \times 10^7 M_\odot$. A virial estimate based on the photoionization method (Wandel, Peterson & Malkan 1999) is $2.2 \times 10^7 M_\odot$. The black hole mass can also be estimated via the well-known relation between stellar velocity dispersion σ_* and M_{BH} . We use equation 19 of Tremaine et al. (2002), $M_{BH} = 10^{8.13 \pm 0.06} M_\odot \times (\sigma_*/(200 \text{ km s}^{-1}))^{4.02 \pm 0.32}$. Oliva et al. (1999) report $\sigma_* = 218 \pm 20 \text{ km s}^{-1}$ or $231 \pm 20 \text{ km s}^{-1}$ using $1.59 \mu\text{m Si}$ or $1.62 \mu\text{m CO}(6,3)$ features, respectively. Using the average of these two values yields $M_{BH} = 2.17_{-1.05}^{+1.98} \times 10^8 M_\odot$. Finally, Nikolajuk, Papadakis & Czerny (2004) suggested a prescription to estimate M_{BH} based on short-term (~ 1 day duration) X-ray variability amplitude measurements, provided that the variability amplitude measured probes temporal frequencies above the PSD break and that the PSD power law slope at high temporal frequencies is -2 ; this assumption is consistent with the current PSD results. Nikolajuk, Czerny & Papadakis (2004) estimated $M_{BH} = 1.24 \times 10^8 M_\odot$ based on short-term *RXTE* light curves, and Markowitz, Reeves & Braitto (2006) estimated $M_{BH} = 8.64 \pm 0.60 \times 10^7 M_\odot$ using a 2.5–12 keV light curve from the 2003 *XMM-Newton* pn observation.

⁴ The ionization parameter $\xi \equiv L_{ion} n_e^{-1} r^{-2}$, where L_{ion} is the isotropic 1–1000 Ryd ionizing continuum luminosity, n_e is the electron number density, and r is the distance from the central continuum source to the absorbing gas.

Several of the X-ray timing studies discussed in §1 have noted the remarkable similarity between Seyferts and black hole X-ray Binaries in terms of their broadband PSD shapes; furthermore, the T_b - M_{BH} - L_{Bol} relation extrapolates down to stellar-mass black holes over 6–7 orders of magnitude in both M_{BH} and X-ray luminosity. However, it is not immediately obvious from the shape of IC 4329a’s PSD and from the derived value of $L_{\text{Bol}}/L_{\text{Edd}}$ if IC 4329a is an analog to a high/soft or low/hard state black hole X-ray Binary system. There is not enough temporal frequency coverage below the break in the PSD of IC 4329a to determine if the power-law slope of ~ -1 persists for several decades of temporal frequency below the break, which would identify it as an analog of Cyg X-1 in the high/soft state (e.g., Axelsson, Borgonovo & Larsson 2005); monitoring covering temporal frequencies down to and below $10^{\sim -9}$ Hz would be needed to determine the ultra-low temporal frequency PSD shape of IC 4329a.

5.2. The energy-dependent PSD properties of IC 4329a

The PSDs presented here are roughly consistent with same underlying broadband PSD shape at all energies probed: a break near 2×10^{-6} Hz, and power-law slopes of ~ -1.0 and ~ -2.0 below and above the break frequency, respectively. The 10–20 and 20–40 keV PSDs are probing temporal frequencies primarily below the break frequency but are consistent with the presence of a break

in the PSD up to 20–40 keV.

Arévalo & Uttley (2006) noted that an increase in f_b with photon energy is expected in a model incorporating inwardly propagating variations in the local mass accretion rate modifying the central X-ray emission (Lyubarskii 1997, Kotov et al. 2001), with relatively harder X-ray bands associated with more centrally concentrated emissivity profiles. However, no significant breaks were detected in the 10–20 and 20–40 keV PSDs. The current 3–5 and 5–10 keV PSDs lack the necessary high temporal frequency resolution to discern any dependence of f_b on photon energy. A much more dense temporal frequency sampling covering at least the range $\sim 10^{-7} - \sim 10^{-4.5}$ Hz would be required to adequately test any energy dependence of f_b in this object.

A.M. thanks the *RXTE* Science Operations staff, particularly the *RXTE* schedulers for ensuring that the long-term monitoring observations were scheduled so evenly all these years. This work has made use of HEASARC online services, supported by NASA/GSFC, the NASA/IPAC Extragalactic Database, operated by JPL/California Institute of Technology under contract with NASA, and the NIST Atomic Spectra Database. A.M. acknowledges financial support from NASA grant NAS5-30720.

REFERENCES

- Arévalo, P. & Uttley, P. 2006, *MNRAS*, 367, 801
 Axelsson, M., Borgonovo, L. & Larsson, S. 2005, *A&A*, 438, 999
 Bautista, M.A. & Kallman, T. 2001, *ApJS*, 134, 139
 Edelson, R. & Nandra, K. 1999, *ApJ*, 514, 682
 Green, A., McHardy, I. & Lehto, H. 1993, *MNRAS*, 265, 664
 Gruber, D.E., Blanco, P.R., Heindl, W.A., Pelling, M.R., Rothschild, R.E. & Hink, P.L. 1996, *A&AS*, 120, 641
 Jahoda, K., Markwardt, C.B., Radeva, Y., Rots, A., Stark, M.J., Swank, J., Strohmayer, T. & Zhang, W. 2006, *ApJS*, 163, 401
 Kalberla, P.M.W. et al. 2005, *A&A*, 440, 775
 Kaspi, S., Smith, P.S., Netzer, H., Maoz, D., Jannuzi, B.T. & Giveon, U. 2000, *ApJ*, 533, 631
 Kotov, O., Churazov, E. & Gilfanov, M. 2001, *MNRAS*, 327, 799
 Lawrence, A., Watson, M., Pounds, K. & Elvis, M. 1987, *Nature*, 325, 694
 Lyubarskii, Y.E. 1997, *MNRAS*, 292, 679
 Marconi, A., Risaliti, G., Gilli, R., Hunt, L.K., Maiolino, R. & Salvati, M. 2004, *MNRAS*, 351, 169
 Markowitz, A., Edelson, R. & Vaughan, S. 2003a, *ApJ*, 598, 935
 Markowitz, A., Edelson, R., Vaughan, S., et al. 2003b, *ApJ*, 593, 96 (M03)
 Markowitz, A., Reeves, J.N., George, I.M., et al., 2009, *ApJ*, 691, 922
 Markowitz, A., Reeves, J.N. & Braitto, V. 2006, *ApJ*, 646, 783
 McHardy, I.M. & Czerny, B. 1987, *Nature*, 325, 696
 McHardy, I.M., Gunn, K.F., Uttley, P. & Goad, M.R. 2005, *MNRAS*, 359, 1469
 McHardy, I.M., Koerding, E., Knigge, C., Uttley, P. & Fender, R.P. 2006, *Nature*, 444, 730
 McHardy, I.M., Papadakis, I.E., Uttley, P., Page, M.J. & Mason, K.O. 2004, *MNRAS*, 348, 783
 Miniutti, G., Fabian, A.C., Anabuki, N., et al. 2007, *PASJ*, 59S, 315
 Mould, J.R., Huchra, J.P., Freedman, W.L., et al. 2000, *ApJ*, 529, 786
 Nevalainen, J., Oosterbroek, T., Bonamente, M. & Colafrancesco, S. 2004, *ApJ*, 608, 166
 Nikolajuk, M., Papadakis, I. & Czerny, B. 2004, *MNRAS*, 350, L26
 Oliva, E., Origlia, L., Maiolino, R. & Moorwood, A.F.M. 1999, *A&A*, 350, 9
 Oppenheim, A. & Shafer, R. 1975, “Digital Signal Processing” (Prentice-Hall Publishing)
 Papadakis, I.E. & Lawrence, A. 1993, *MNRAS*, 261, 612
 Papadakis, I.E., Reig, P. & Nandra, K. 2003, *MNRAS*, 344, 993
 Peterson, B.M., Ferrarese, L., Gilbert, K.M., et al. 2004, *ApJ*, 613, 682
 Pounds, K., Edelson, R., Markowitz, A., & Vaughan, S. 2001, *ApJ*, 550, L15
 Revnivtsev, M., Sazonov, S., Jahoda, K. & Gilfanov, M. 2004, *A&A*, 418, 927
 Rothschild, R., Blanco, P.R., Gruber, D.E., Heindl, W.A., MacDonald, D.R., Marsden, D.C., Pelling, M.R. & Wayne, L.R. 1998, *ApJ*, 496, 538
 Steenbrugge, K.C., Kaastra, J.S., Sako, M., Branduardi-Raymont, G., Behar, E., Paerels, F.B.S., Blustin, A.J. & Kahn, S.M. 2005, *A&A*, 432, 453
 Swank, J. 1998, in *Nuclear Phys. B (Proc. Suppl.): The Active X-ray Sky: Results From BeppoSAX and Rossi-XTE*, Rome, Italy, 1997 October 21–24, eds. L. Scarsi, H. Bradt, P. Giommi, & F. Fiore, *Nucl. Phys. B Suppl. Proc. (The Netherlands: Elsevier Science B.V.)*, 69, 12
 Timmer, J. & König, M. 1995, *A&A*, 300, 707
 Tremaine, S., Gebhardt, K., Bender, R., et al. 2002, *ApJ*, 574, 740
 Uttley, P. & McHardy, I.M. 2005, *MNRAS*, 363, 586
 Uttley, P., McHardy, I.M. & Papadakis, I.E. 2002, *MNRAS*, 332, 231 (U02)
 Vaughan, S. 2005, *A&A*, 431, 391
 Vaughan, S., Edelson, R., Warwick, R. & Uttley, P. 2003, *MNRAS*, 345, 1271
 Vestergaard, M. & Peterson, B.M. 2006, *ApJ*, 641, 689
 Wandel, A., Peterson, B.M. & Malkan, M. 1999, *ApJ*, 526, 579
 Willmer, C.N.A., Focardi, P., Chan, R., Pilligrini, P.S. & Nicolaci da Costa, L. 1991, *AJ*, 101, 57
 Winge, C., Peterson, B.M., Pastoriza, M.G. & Storchi-Bergmann, T. 1996, *ApJ*, 469, 648

TABLE 1
LIGHT CURVE SAMPLING PARAMETERS

Bandpass (keV)	Time scale	Instrument	ΔT_{samp}	Mean Source Flux ($\text{erg cm}^{-2} \text{ s}^{-1}$)	Mean Source Count Rate ct s^{-1}	Mean Background Count Rate ct s^{-1}	F_{var} (%)
3–10	Long	PCA	4.26 d	11.18×10^{-11}	11.57	2.99	17.28 ± 0.08
	Medium	PCA	17.1 ks	9.72×10^{-11}	10.12	2.98	8.69 ± 0.17
	Short	pn	3000 s	7.63×10^{-11}	4.86	0.03	3.72 ± 0.16
3–5	Long	PCA	4.26 d	4.22×10^{-11}	4.94	1.05	18.61 ± 0.12
	Medium	PCA	17.1 ks	3.60×10^{-11}	4.28	1.05	9.95 ± 0.22
	Short	pn	5000 s	2.83×10^{-11}	2.77	0.02	4.01 ± 0.21
5–10	Long	PCA	4.26 d	6.96×10^{-11}	6.63	1.94	16.47 ± 0.11
	Medium	PCA	17.1 ks	6.12×10^{-11}	5.84	1.94	8.34 ± 0.23
	Short	pn	5000 s	4.77×10^{-11}	2.06	0.01	3.17 ± 0.27
10–20	Long	PCA	4.26 d	8.22×10^{-11}	2.33	2.15	15.07 ± 0.21
	Medium	PCA	17.1 ks	7.33×10^{-11}	2.07	2.14	7.53 ± 0.53
20–40	Long	HEXTE	12.79 d	8.38×10^{-11}	0.32	3.54	17.03 ± 1.19
	Medium	HEXTE	50.2 ks	8.07×10^{-11}	0.31	3.44	12.82 ± 1.31

NOTE. — ΔT_{samp} is the sampling interval. PCA count rates are for one PCU. For the HEXTE light curves, count rates are per detector, taking into account the number of good detectors per cluster and observations where cluster A data were not used. PCA fluxes were determined from fitting simple power-law models over the given energy range.

TABLE 2
PSD MEASUREMENT PARAMETERS

Bandpass (keV)	Time- scale	Temporal Frequency Range Spanned (Hz)	P_{Psn} (Hz^{-1})
3–10	Long	$1.26 \times 10^{-8} - 1.06 \times 10^{-6}$	80.1
	Medium	$5.83 \times 10^{-7} - 2.30 \times 10^{-5}$	4.27
	Short	$1.29 \times 10^{-5} - 1.81 \times 10^{-4}$	0.41
3–5	Long	$1.26 \times 10^{-8} - 1.06 \times 10^{-6}$	181
	Medium	$5.83 \times 10^{-7} - 2.30 \times 10^{-5}$	9.72
	Short	$1.28 \times 10^{-5} - 6.30 \times 10^{-5}$	0.72
5–10	Long	$1.26 \times 10^{-8} - 1.06 \times 10^{-6}$	144
	Medium	$5.83 \times 10^{-7} - 2.30 \times 10^{-5}$	7.62
	Short	$1.28 \times 10^{-5} - 6.30 \times 10^{-5}$	0.98
10–20	Long	$1.26 \times 10^{-8} - 1.06 \times 10^{-6}$	608
	Medium	$5.83 \times 10^{-7} - 2.30 \times 10^{-5}$	32.8
20–40	Long	$1.25 \times 10^{-8} - 3.50 \times 10^{-7}$	5940
	Medium	$5.75 \times 10^{-7} - 7.41 \times 10^{-6}$	180

NOTE. — P_{Psn} is the power due to Poisson noise (see text for details).

TABLE 3
UNBROKEN POWER LAW MODEL FITS TO PSDS

Bandpass (keV)	α	A_0 (Hz^{-1})	L_{unbr} (%)
3–10	$1.7^{+0.4}_{-0.3}$	$2.5 \pm 0.5 \times 10^3$	2.2
3–5	$1.5^{+0.4}_{-0.2}$	$3.0^{+0.4}_{-0.3} \times 10^3$	9.4
5–10	$1.5^{+0.5}_{-0.2}$	$2.3^{+0.3}_{-0.2} \times 10^3$	4.0
10–20	1.2 ± 0.2	$2.1 \pm 0.2 \times 10^3$	17.5
20–40	1.1 ± 0.3	$5.5^{+0.9}_{-0.8} \times 10^3$	22.3

NOTE. — Results from fitting the PSDs with unbroken power law model. A_0 is the amplitude at $f = 10^{-6}$ Hz. L_{unbr} is the likelihood of acceptance for this model, defined as one minus the rejection probability.

TABLE 4
BROKEN POWER LAW MODEL FITS TO PSDS

Bandpass (keV)	α_{lo}	f_b (Hz)	α_{hi}	A_1 (Hz $^{-1}$)	L_{brkn}	L_{brkn}/L_{unbr}
3–10	$1.0^{+0.4}_{-0.3}$	$2.51^{+2.50}_{-1.72} \times 10^{-6}$	$2.3^{+0.8}_{-0.4}$	$1.8 \pm 0.2 \times 10^3$	87.8	39.9
3–5	$0.6^{+0.5}_{-0.6*}$	$2.51^{+0.65}_{-1.51} \times 10^{-7}$	$1.7^{+0.2}_{-0.3}$	$4.5^{+0.5}_{-0.4} \times 10^4$	97.1	10.3
	1.0(fixed)	$7.94^{+12.06}_{-6.36} \times 10^{-7}$	$1.7^{+0.5}_{-0.2}$	$7.5 \pm 0.7 \times 10^3$	90.4	9.6
5–10	$1.1^{+0.3}_{-0.2}$	$3.16^{+3.15}_{-2.53} \times 10^{-6}$	$2.0^{+0.6}_{-0.3}$	$9.5 \pm 0.9 \times 10^2$	82.5	20.6
	1.0 (fixed)	$1.00^{+2.16}_{-0.75} \times 10^{-6}$	$1.8^{+0.3}_{-0.2}$	$4.6^{+0.5}_{-0.4} \times 10^3$	79.2	19.8
10–20	$(1.1^{+0.1}_{-0.2})$	$(1.26^{+0*}_{-0.63} \times 10^{-5})$	(1.70)	$(3.8^{+0.6}_{-0.5} \times 10^2)$	(29.4)	(1.7)
20–40	$(0.7^{+0.3}_{-0.7*})$	$(3.16^{+28.44}_{-2.53} \times 10^{-7})$	$(1.4^{+0.2}_{-0.4})$	$(4.4^{+1.0}_{-0.8} \times 10^3)$	(75.9)	(3.4)

NOTE. — Results from fitting the PSDs with a broken power law model. A_1 is the amplitude at the break frequency f_b ; α_{lo} and α_{hi} are the power law slopes below and above f_b , respectively. L_{brkn} is the likelihood of acceptance for this model, defined as one minus the rejection probability. An asterisk (*) denotes that the parameter uncertainty pegged at the limit of the parameter space tested. Best-fit parameters for the 10–20 and 20–40 keV PSDs are in parentheses, as the broken power-law model fits do not provide a statistically significant improvement over the unbroken power-law model fits. For the 10–20 keV PSD, the best-fit break frequency is located near the edge of the temporal frequency range sampled, so no reasonable constraints on α_{hi} are obtained.

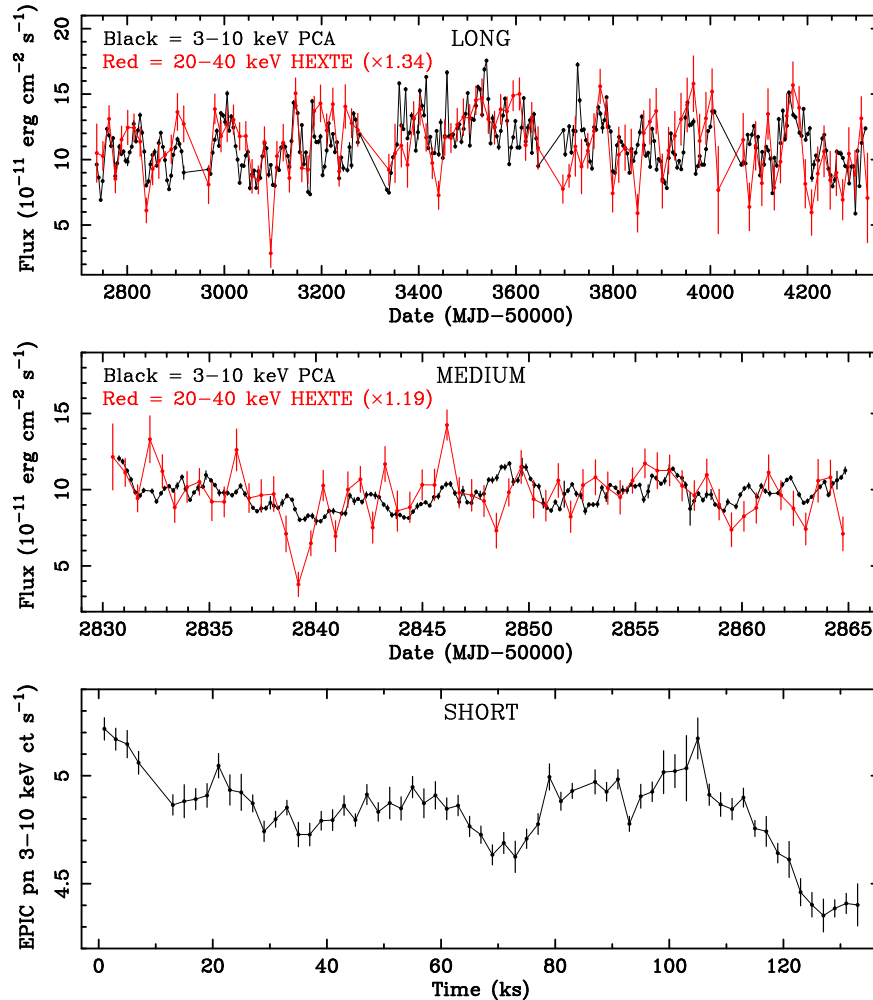


FIG. 1.— Long-, medium-, and short-term light curves of IC 4329a. The top (middle) panel shows the long- (medium-) term 3–10 keV PCA and 20–40 keV HEXTE flux light curves (the latter curves renormalized to the mean of the PCA light curves). The lower panel shows the 3–10 keV short-term EPIC pn light curve binned to 2000 s and in units of EPIC pn ct s $^{-1}$.

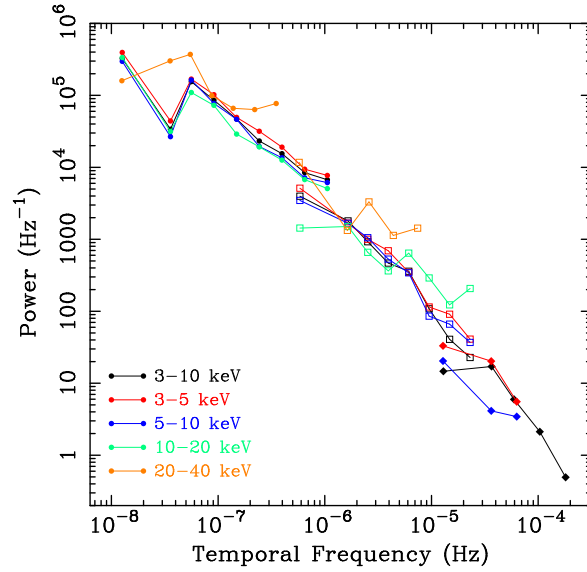


FIG. 2.— The observed PSDs for the 3–10 (black), 3–5 (red), 5–10 (blue), 10–20 (green), and 20–40 keV (orange) PSDs. Filled circles, open squares, and filled diamonds denote PSDs derived from long-, medium-, and short-term monitoring, respectively.

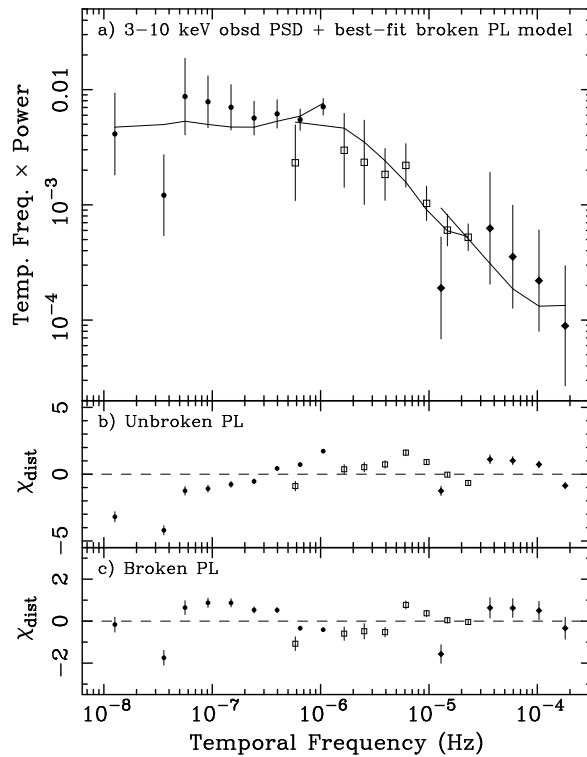


FIG. 3.— The top panel shows the observed 3–10 keV PSD, plotted in $f \times P(f)$ space to visually emphasize the turnover. Filled circles, open squares, and filled diamonds denote PSDs derived from long-, medium-, and short-term monitoring, respectively. The solid line denotes the best-fit singly-broken power-law model folded through the sampling window (i.e., containing the distortion effects of PSD measurement and power due to Poisson noise). The middle and bottom panels show the residuals to the best-fit unbroken and broken power law models, respectively.

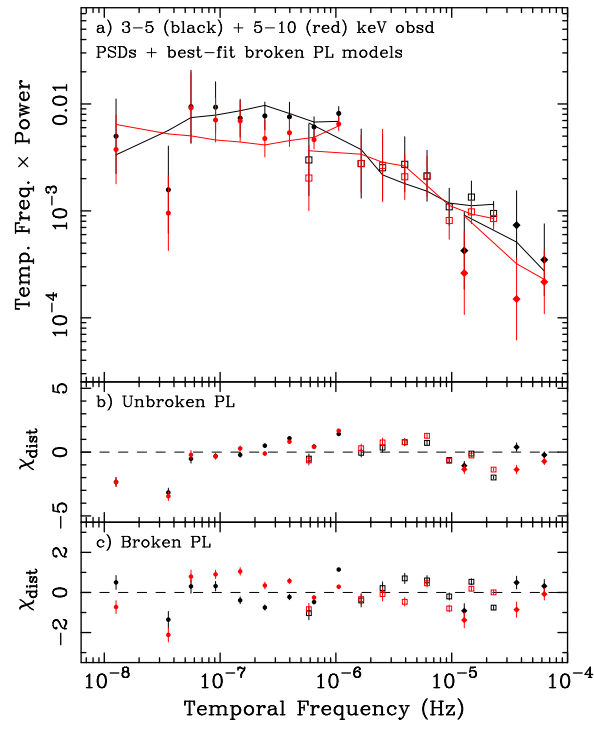


FIG. 4.— Same as Figure 3, but for the 3–5 (black) and 5–10 (red) keV PSDs.

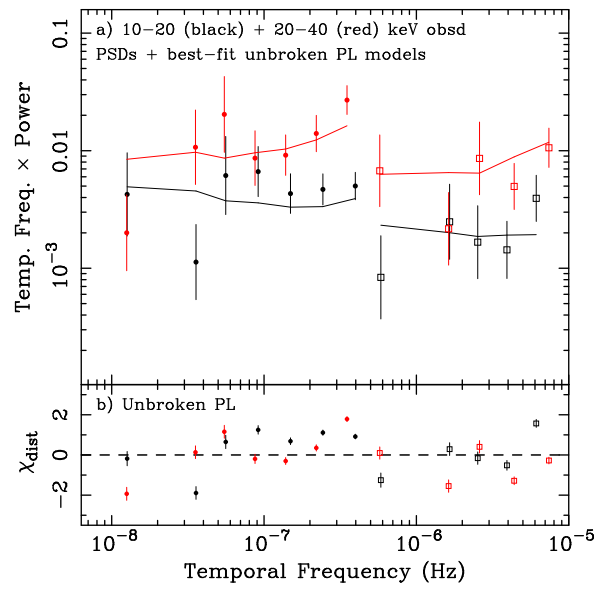


FIG. 5.— The top panel shows the observed 20–40 keV PSD; symbols are the same as in Figure 3. The solid line denotes the best-fit “distorted” unbroken power-law model. The bottom panel shows the residuals to the best-fit unbroken power law model.

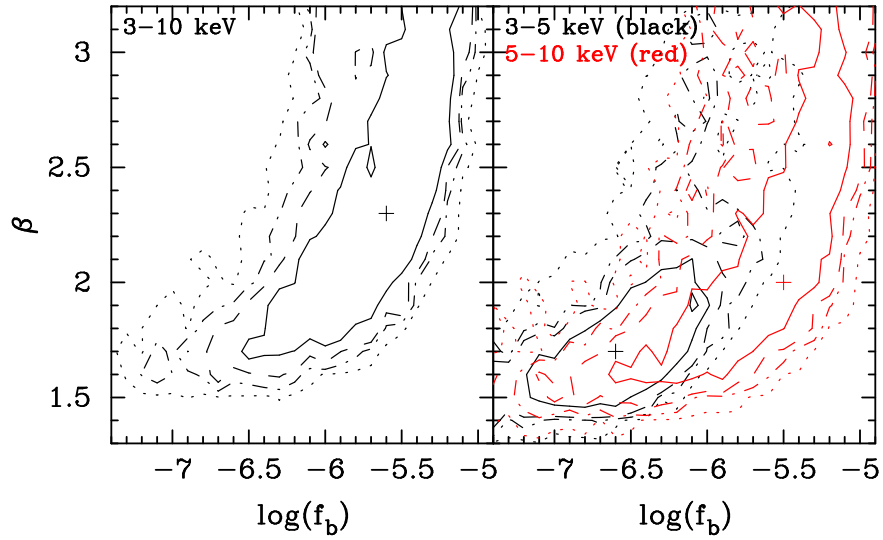


FIG. 6.— Contour plots of α_{hi} versus f_b for the best-fit singly broken power-law models for the 3–10 (left panel), 3–5 (right panel; black contours) and 5–10 (right panel; red contours) keV PSDs. Each contour represents a slice through the parameter space tested at the best-fit value of α_{lo} (listed in Table 4). Solid, dashed, dot-dashed, and dotted contours denote 68, 90, 95.4, and 99.0% rejection probabilities, respectively.